PAPER

Check for updates

Regenerable chitosan-embedded magnetic iron oxide beads for nitrate removal from industrial wastewater†

Muntaha Nasir,[a] Farhan Javaid, [ID][a] M. Talha Masood,[a] Dr Muhammad Arshad, [ID][b] Muhammad Yasir, [ID][c] Vladimir Sedlarik,[c] Muhammad Abdel Qadir,[d] Hazim Qiblawey, [ID][e] Wenjuan Zhang,[f] Kashif Mairaj Deen, [ID]*[g] Edouard Asselin[g] and Nasir M. Ahmad*[a]

Industrial sites worldwide significantly contribute to water pollution. Nitrates are a common effluent pollutant from such sites. Effective means to remove nitrate ions (NO_3^-) from polluted waters are needed. Chitosan beads, which are a non-toxic, biocompatible, and biodegradable polymer, are used for this purpose in this research. Iron-oxide nanoparticles are synthesized *via* the co-precipitation route and embedded into chitosan by chemical co-precipitation to form ion exchange chitosan beads (IECBs) for NO_3^- removal. The performance of the IECBs in a batch system was studied against NO_3^- adsorption from industrial water. Morphological, structural, and chemical characterization was performed by SEM, EDX mapping, BET, XRD, and FTIR, while the extent of NO_3^- adsorption was quantified using UV-vis spectroscopy. Different factors influencing the adsorption of NO_3^- on the IECBs were investigated, including the adsorbent dosage, pH of the solution, initial concentration, and interaction time. It is demonstrated that pseudo-second-order isothermal and kinetic models were best fits to the experimental data. It was found that the IECBs had a maximum adsorption capacity of 47.07 mg g^{-1} and could load up to ~93% of the NO_3^- from the batch system. The regeneration efficiency for the IECBs over 5 cycles remained high in the range of 93% to 79%, indicating their potential for industrial water treatment use.

Environmental significance

This study introduces ion exchange chitosan beads (IECBs) for efficient removal of nitrate ions (NO_3^-) from industrial wastewater. Combining chitosan with synthesized iron-oxide nanoparticles, IECBs exhibit a high adsorption capacity of 47.07 mg g^{-1} and achieve a notable removal efficiency of ~93%. Pseudo-second-order models best fit the isothermal and kinetic data. Successful regeneration over five cycles further highlights their potential as a sustainable solution for eco-friendly industrial water treatment.

[a]Polymer Research Lab, School of Chemical and Materials Engineering (SCME), National University of Sciences and Technology (NUST), H-12, Islamabad, Pakistan. E-mail: nasir.ahmad@scme.nust.edu.pk

[b]Institute of Environmental Science and Engineering (IESE), National University of Sciences and Technology (NUST), H-12, Islamabad, Pakistan

[c]Centre of Polymer Systems, University Institute, Tomas Bata University in Zlín, Třída Tomáše Bati 5678, 76001 Zlín, Czech Republic

[d]School of Chemistry, The University of the Punjab, Lahore 54590, Pakistan

[e]Department of Chemical Engineering, College of Engineering, Qatar University, Qatar

[f]State Key Laboratory of Advanced Metallurgy, University of Science and Technology Beijing, Beijing 100083, China

[g]Department of Materials Engineering, The University of British Columbia, Vancouver, V6T 1Z4, BC, Canada. E-mail: kashifmairaj.deen@ubc.ca

† Electronic supplementary information (ESI) available. See DOI: https://doi.org/10.1039/d3va00351e

1 Introduction

A significant problem that has rapidly spread worldwide, attributed to limited water supplies, industrialization, and population growth, is the shortage of clean water. Consequently, one strategy to address this shortfall is to treat industrial wastewater, removing pollutants released regularly through various physical, chemical, and biological procedures. This approach facilitates the creation of clean water on a large scale, suitable for both industrial and agricultural purposes. Nitrate, due to its high solubility in water, is a widespread contaminant in both surface and groundwater. In recent years, there has been increased awareness of nitrate contamination, elevating it to a major global environmental issue.[1] The primary sources of nitrates in groundwater are fertilizers, septic tanks, and manure storage or industrial application processes, which

cause nitrate discharge as a waste product.[2] Nitrogen from fertilizer that is not absorbed by the plants, volatilized, or removed by surface runoff eventually ends up as nitrates in water. Subsequently, the nitrogen becomes inaccessible for the plants, and its concentration in the groundwater may increase above the acceptable limits for safe drinking water, which is 10 mg L^{-1}.[3,4] Fields, barnyards, and storage areas can all be sources of anthropogenic nitrogen.[5] Long-term exposure to excessive nitrate levels can result in the extinction of some species and, thus, disturbance of entire ecosystems. Cancer, thyroid illness, blue baby syndrome, and other acute problems may result from nitrate water contamination. Hence, removing nitrates from water is very important to avoid all associated dangers.[6]

Diverse technologies and methods are under development for nitrate contaminant removal from wastewater.[7] These methods encompass physicochemical removal,[8,9] ion exchange technologies,[10,11] electrochemical reduction,[12,13] reverse osmosis,[14] electrochemical oxidation,[15] electro-coagulation,[16] thermal decomposition,[17,18] the polyol method,[19] adsorption methods,[20] and biological denitrification.[21] Within this spectrum, some technologies necessitate pretreatment to prevent membrane and resin fouling, while others incur higher costs.

Among these methods, adsorption stands out as one of the most effective, efficient, and straightforward approaches for nitrate ion removal. Recently, adsorption has gained prominence as the most promising method for wastewater treatment thanks to its affordability, environmental friendliness, ease of use, flexibility, absence of byproducts, potential for adsorbent regeneration, and minimal pretreatment requirements.[22]

In addressing the challenge of nitrate contaminant removal, a variety of adsorbents, such as fly ash, carbon, clay, activated carbon, nano-alumina, carbon nanotubes, and chitosan, have been investigated.[23] Chitosan, derived from a straightforward deacetylation process of chitin found in resources like shrimp, crabs, fungi, and insects, stands out as a cationic biopolymer widely recognized for its exceptional adsorption capabilities in removing harmful ions from wastewater.[24] While existing literature reveals the highest reported nitrate adsorption capacity using modified chitosan microspheres to be 32.15 mg g^{-1}[25] limited studies have explored nitrate removal using iron oxide embedded chitosan beads, indicating a potential research gap in this area. Leveraging the abundance, biodegradability, non-toxicity, and biocompatibility of chitosan as a natural polymer, our study aims to contribute novel insights into its effectiveness for nitrate removal.[26] Chitosan possesses functional amino and hydroxyl groups in its backbone. In its pure form, chitosan lacks mechanical stability. To enhance its mechanical properties, we also modified the beads through functionalization and incorporation of iron oxide (Fe_3O_4) nanoparticles.[27] These magnetic beads introduced into wastewater attract nitrate ions through electrostatic interactions and chemical bonding involving hydroxyl and amino functional groups on their surface. This mechanism holds the nitrate ions on the beads *via* adsorption and offers a relatively environmentally friendly solution. Nitrate removal efficiency with magnetic beads depends on various factors such as bead size, surface area, adsorbent material, wastewater pH, and nitrate ion concentration.

In this study, we synthesized Fe_3O_4 nanoparticles through co-precipitation and subsequently incorporated them into chitosan using polyvinylpyrrolidone (PVP) as a crosslinker. This facilitated the formation of a robust bond between chitosan and Fe_3O_4 (magnetite) nanoparticles, resulting in the synthesis of functionalized magnetic beads. This study encompassed batch adsorption experiments aimed at optimizing conditions for the effective removal of nitrate ions. Variables such as the initial pH of wastewater, adsorption time, initial nitrate concentration, and adsorbent dosage were systematically explored. Additionally, the nitrate adsorption capacity of these ion-exchange chitosan beads (IECBs) was evaluated over five cycles of reuse.

2 Materials and methods

2.1 Materials

Iron(III) chloride hexahydrate ($FeCl_3 \cdot 6H_2O$) ($M_w = 270.30$) and iron(II) chloride tetrahydrate ($FeCl_2 \cdot 4H_2O$) ($M_w = 198.81$) were purchased from Duskan reagents, China. Sodium nitrate ($NaNO_3$), chitosan ($C_6H_{11}NO_4$)$_n$, (84% of deacetylation, $M_w = 500\,000$), polyvinylpyrrolidone (PVP), sodium chloride (NaCl), magnesium chloride ($MgCl_2$), sodium sulfate (Na_2SO_4), sodium hydroxide (NaOH) (pellets 98%, anhydrous), acetic acid (CH_3-COOH) (glacial 99–100%) and hydrochloric acid (HCl) were obtained from Sigma-Aldrich, Germany. Ammonia (NH$_4$OH-32%) was bought from Merck, South Korea. All the reagents and solvents used in this investigation were of analytical grade and were utilized without further purification.

2.2 Synthesis of magnetic beads

2.2.1 Step 1: preparation of iron oxide nanoparticles. The co-precipitation process[28] was used to synthesize Fe_3O_4 nanoparticles as schematically shown in Fig. 1a. 8 mmol of $FeCl_3 \cdot 6H_2O$ and 4 mmol of $FeCl_2 \cdot 4H_2O$ were dissolved in 100 mL of deionized water at 20 °C. Each time, 5 mL of aqueous ammonium hydroxide solution (NH$_4$OH-32%) was added promptly while stirring. Upon the addition of NH$_4$OH, precipitation commenced, causing the solution's color to change from pale yellow to dark as the precipitates were formed. After the precipitation was complete, the precipitates were allowed to settle down, and the supernatant solution was decanted.[29] The dark brown precipitates were recovered and thoroughly washed with deionized water and propanol. They were then separated from the solution using centrifugation at 200 rpm for 2 h. The resulting clean precipitates were dried overnight at 60 °C in a vacuum oven. Subsequently, any agglomerated precipitates were manually ground using a mortar and pestle.[30]

2.2.2 Step 2: formation of iron oxide embedded chitosan beads. IECBs were synthesized using the embedding method, as discussed elsewhere.[31] Meanwhile, Fe_3O_4 nanoparticles were prepared using co-precipitation prior to this (as mentioned in Section 2.2.1).[32] To create hybrid beads, 2.6% v/v acetic acid was added into a 50 mL solution containing 3.5 g of chitosan while continuously stirring for 12 h at 450 rpm. 1 g of Fe_3O_4
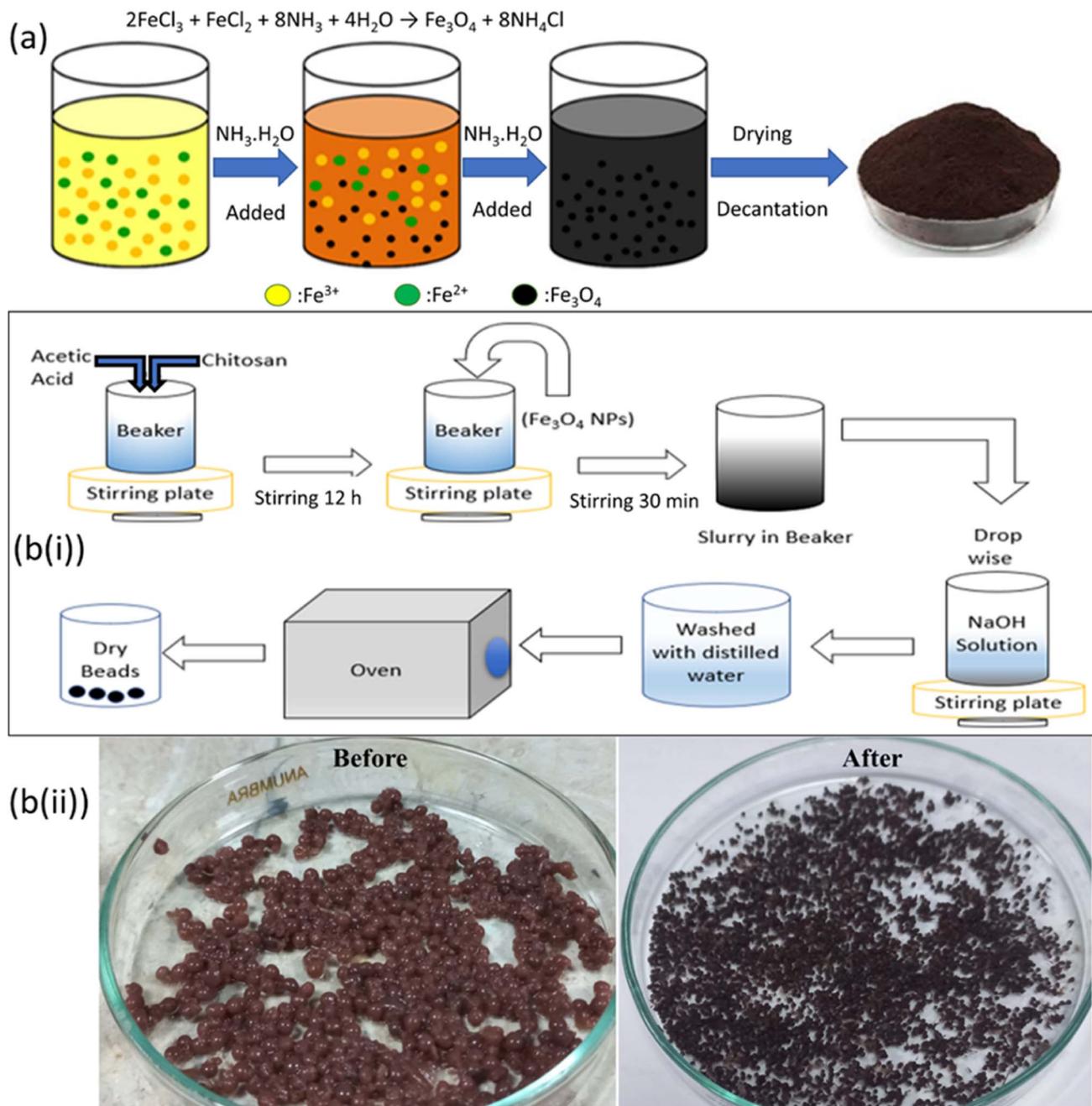
Fig. 1 (a) Illustration of synthesis of Fe_3O_4 nanoparticles, and (b) representation of the synthesis of magnetic chitosan beads; (i) flow-chart scheme; (ii) images of synthesized beads before and after drying.

nanoparticles was then added to this solution after it became viscous. The final solution was then further agitated by sonication (for 30 min) to make it even more viscous, homogeneous, and air-free.[33] Using a syringe, the resultant slurry of chitosan-iron oxide was added dropwise into 1 M NaOH solution while continuously stirring.[31] Then, hybrid chitosan-iron oxide beads were removed from the NaOH solution and repeatedly submerged in water until the filtrate's pH was neutral. In the end, beads were dried in a vacuum oven at 65 °C for 4 h.[34] All these steps have been illustrated as a flow chart in Fig. 1b(i). The

actual images of beads before and after drying are also presented in Fig. 1b(ii).

2.3 Characterization techniques and performance evaluation

The morphology of the synthesized Fe_3O_4 nanoparticles and magnetic beads was imaged using scanning electron microscopy (SEM) JSM 67001 (JEOL, Japan) at an accelerating voltage of 10–20 kV. Compositional mapping was done with energy dispersive spectroscopy (EDX) (JEOL, Japan). The crystal

structure of the Fe$_3$O$_4$ nanoparticles and IECBs was examined by X-ray diffraction (XRD) using a D2 PHASER (Bruker, Germany), with Cu Kα radiation at a wavelength of $\lambda = 1.54$ Å and a scan rate of 0.02 s^{-1}. FTIR was performed on a Perkin-Elmer-283B spectrometer (USA), in the range of 400 to 4000 cm^{-1} at a resolution of 4 cm^{-1} to confirm the presence of –OH and –NH functional groups associated with magnetic chitosan beads comprising the Fe$_3$O$_4$ nanoparticles. In addition, FTIR was used to identify N–O bond vibrations to confirm nitrate adsorption. The surface area and average pore size of the beads were measured by N$_2$ adsorption at 77 K using the Brunauer–Emmett–Teller (BET) method with an ASAP 2420 system (Micromeritics, USA). The laser diffraction analysis of the as-synthesized iron oxide nanoparticles was carried out by using a Mastersizer 3000. Before diffraction analysis, the iron oxide nanoparticles were ultrasonicated for 5 s to dissociate the agglomerated particles. The magnetic properties of the IECBs were measured using a vibrating sample magnetometer (DXV 220, DEXING) equipped with JDAW 2000 software. A fine powder sample made by manual grinding was placed in a sample holder under room conditions and analyzed under an external magnetic field between −5 and +5 kOe. Prior to the adsorption studies, samples were degassed at 110 °C for 1 h using a degassing chamber (Micromeritics, VacPrep 061). Nitrate adsorption was analyzed throughout the batch study using ultra-violet radiation spectroscopy using an Agilent 8453 spectrophotometer (JENWAY, UK), operating within the 200–800 nm wavelength range.

2.4 Adsorption capacity and nitrate removal efficiency

For each adsorption experiment, 180 mg of beads were added to 1 L of nitrate water and mechanically agitated for 2 h. A shaker was used to impose continuous stirring and to extract the nitrate with the Fe$_3$O$_4$-embedded chitosan beads. The samples were taken from the solution at different intervals, and the beads were removed by centrifugation. The nitrate ion concentration was determined following the Beer–Lambert law using UV-vis spectroscopy. The remaining nitrate concentration was measured to calculate adsorption capacity and removal efficiency and determine the maximum adsorption of nitrate ions on the beads. The following relationship in eqn (1) is used to determine the capacity of the adsorbent to bind nitrate.[35,36]

$$Q_e = \frac{(C_O - C_e)}{m} \times v \tag{1}$$

Here in this equation, Q_e is adsorption capacity (mg g^{-1}), C_O and C_e are initial and final concentrations (mg L^{-1}), v is the volume of the mixture in liters (L), and m is the mass of magnetic beads. The following formula in eqn (2) is used to determine removal efficiency:

$$\eta(\%) = \frac{(C_O - C_e)}{C_O} \times 100 \tag{2}$$

For the optimization study to determine the best parameters for nitrate removal, we discussed a single parameter change that includes the change in pH (3–9), initial concentration (10–

60 mg L^{-1}), dosage of beads (30–110 mg) and time of contact (160 min) between the beads and nitrate, ions. Using the optimized parameters, the ability of IECBs to remove nitrates was investigated in 100 mL of 50 mg L^{-1} nitrate at 70 mg of IECBs at room temperature. This slurry was agitated at 200 rpm for 2 h.

2.5 Adsorption isotherms

The equilibrium relation between the amount of adsorbate on the adsorbent surface at a constant temperature and the concentration or pressure of the adsorbate in the surrounding phase is known as the adsorption isotherm.[37] To evaluate the mechanism of the adsorption process, it is essential to analyze the isothermal models that best fit the experimental data.[3]

The Langmuir isotherm model is based on some assumptions such as adsorption of a molecule on the surface of the adsorbent due to chemisorption and localized adsorption of adsorbate molecules on the active sites of the adsorbent in single layer. The Langmuir isotherm model is only valid in the case of homogeneous adsorption (of the adsorbate on the adsorbent).[9] The Freundlich model represents non-ideal adsorption and is suitable for heterogeneous surfaces, multi-layered adsorption, and distribution of energy with overactive affinity sites. The Freundlich adsorption isotherm model in eqn (4) is for complex adsorption and heterogeneous surfaces.[6]

$$q_e = \frac{Q_{max} K_L C_e}{(1 + K_L C_e)} \tag{3}$$

$$q_e = K_F C_e^{1/n} \tag{4}$$

C_e is the concentration of the adsorbent at equilibrium (mg L^{-1}), K_L is the Langmuir constant, Q_{max} is the maximum amount of the adsorbent for monolayer adsorption (mg g^{-1}), q_e is the extent of adsorption or amount of nitrate ions adsorbed per unit mass of the adsorbent (mg g^{-1}), K_F is the Freundlich constant, and n is the Freundlich exponent.

2.6 Adsorption kinetics

The sorption kinetics can be modeled using pseudo-first-order or pseudo-second-order processes to determine the adsorption mechanism, as per eqn (5) and (6), respectively.[38]

$$q_t = q_e(1 - e^{-k_1 t}) \tag{5}$$

$$\frac{t}{q_t} = \frac{1}{k_2 q_e^2} + \frac{t}{q_e} \tag{6}$$

where q_t is the adsorbent adsorbed at a time 't' (mg g^{-1}), k_1 is the rate constant of pseudo-first order (l min^{-1}), and k_2 is the pseudo-second-order rate constant g (mg^{-1} min^{-1}).[39]

2.7 Reusability

In a beaker containing 500 mg of aqueous nitrate solution (with 10 mg L^{-1} concentration), 200 mg of IECBs was agitated at 200 rpm for 2 h at room temperature at pH 5.5. The beads were then thoroughly cleaned to remove the adsorbed nitrate ions from their surface. The nitrate-loaded beads underwent stirring

© 2024 The Author(s). Published by the Royal Society of Chemistry

Environ. Sci.: Adv., 2024, **3**, 572–584 | **575**

for 24 h at 200 rpm and room temperature in 250 mL of 0.1 M NaOH solution. This facilitated the elution of chemically bonded nitrate ions from the beads into the solution, ensuring comprehensive cleaning for subsequent reuse. Subsequently, the beads were rinsed with deionized water until reaching a neutral pH and then dried in an oven at 60 °C for 4 hours in preparation for reuse in another loading cycle.

3 Results and discussion

3.1 Morphological studies

The SEM images of the as-synthesized Fe_3O_4 nanoparticles are shown in Fig. 2a and b. Agglomerates of Fe_3O_4 nanoparticles larger than 1 μm are visible in these SEM images. These agglomerates were composed of fine particles that have rough and porous structures as evaluated from the Brunauer–Emmett–Teller (BET) analysis. The total surface area and total pore volume of the synthesized Fe_3O_4 nanoparticles are reported to be 68.723 m^2 g^{-1} and 0.03 cm^3 g^{-1}, respectively. The laser diffraction analysis of the nanoparticles indicated an average particle size of 35.7 nm. This agglomeration is brought on by the steric interaction between the active sites on the surface of these nanoparticles. The agglomeration is due to the magnetic interaction of Fe_3O_4 nanoparticles.[40] Fig. 2c shows that the IECBs have an elliptical shape that is almost spherical. The calculated dimensions from the image of these magnetized chitosan beads range between 1.09 mm and 1.30 mm. Fig. 2d shows that their surface is rough and slightly porous, as also

evident from the BET total area of pores (0.081 m^2 g^{-1}) with a mean pore width of 1.445 nm and a total pore volume of 9 × 10^{-5} cm^3 g^{-1}. This porous surface is consistent with good ion adsorption capacity.[41] The cross-linking of Fe_3O_4 nanoparticles with the hydroxyl and amine groups of the chitosan (using PVP as the crosslinker) is demonstrated by the numerous folds in Fig. 2d. The SEM observations are consistent with the BET results in that the surface area of the Fe_3O_4 nanoparticles is 167.8606 ± 0.9052 m^2 g^{-1}, much higher than that of beads (0.2304 ± 0.0436 m^2 g^{-1}).

3.2 EDX mapping

Fig. S1† shows that there is a significant increase in the nitrogen peak intensity, which clearly indicates the adsorption of nitrate ions onto the IECB surface. The elemental values in the chart are also represented in the ESI (Table S1).†

3.3 Crystal structure: XRD

To confirm the successful synthesis of Fe_3O_4 nanoparticles, their crystal structure was investigated using XRD. Fig. 3a displays the XRD diffractograms of the Fe_3O_4 nanoparticles prepared *via* co-precipitation. The crystalline peaks for Fe_3O_4 were observed at $2\theta = 30.15°$, $35.55°$, $43.1°$, $56.97°$, and $62.55°$, which originated from the characteristic planes of (311), (400), (422), (511), and (440), respectively as per JCPDS card 00-001-1111. However, the broadening of major peaks in the XRD
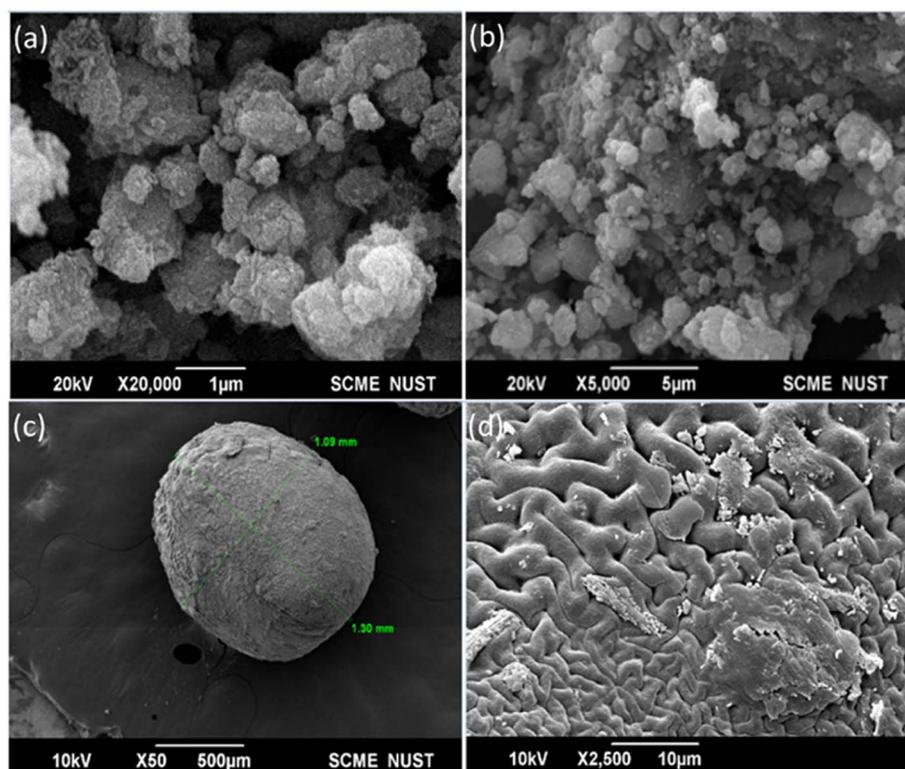

Fig. 2 SEM images of the as-synthesized (a and b) Fe_3O_4 nanoparticles and (c) magnetic chitosan beads (IECBs) and (d) surface morphology of the IECB.
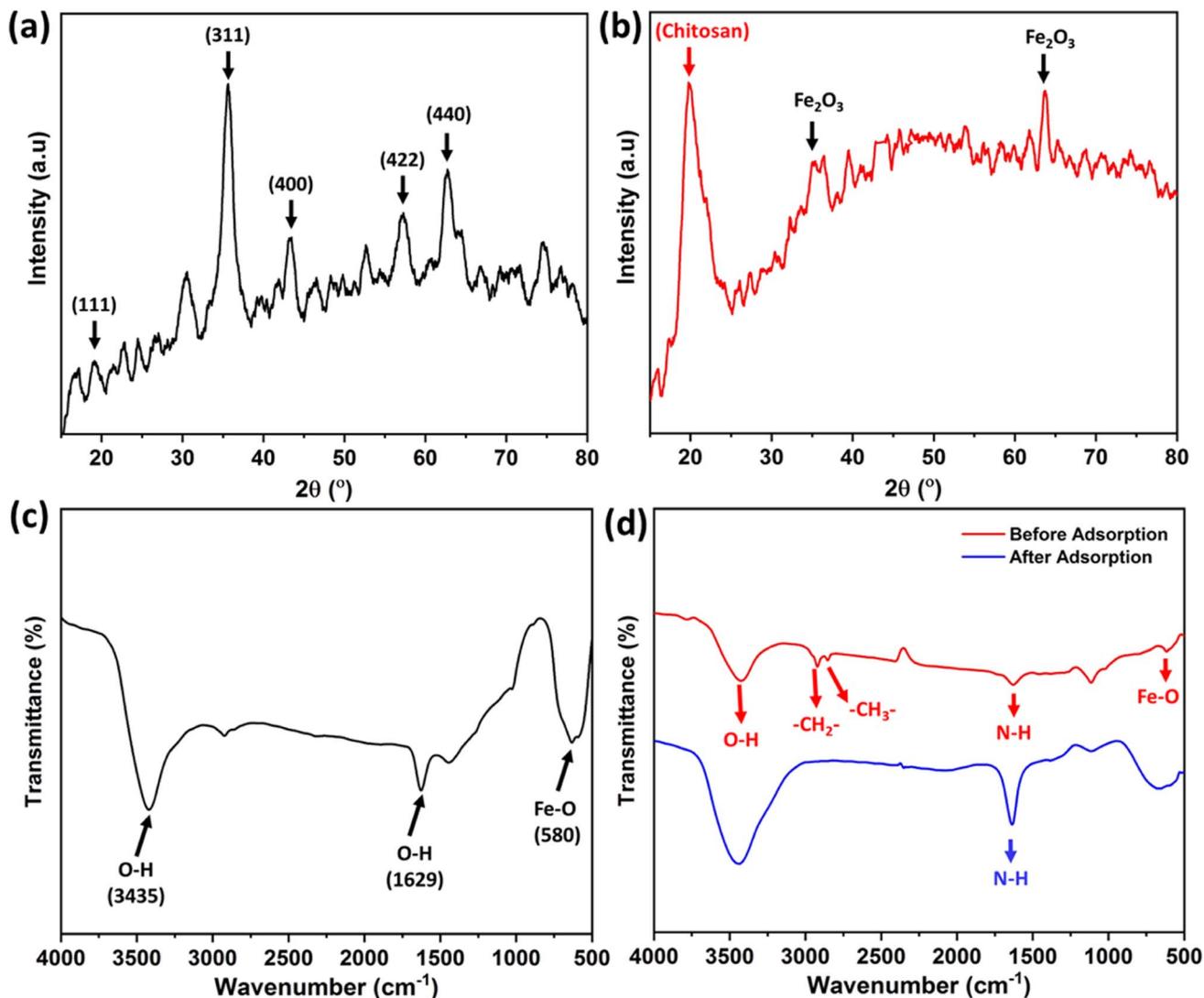
Fig. 3 XRD pattern of (a) Fe_3O_4 nanoparticles and (b) magnetic chitosan beads (IECBs). FTIR spectra of (c) as-synthesized Fe_3O_4 nanoparticles and (d) magnetic chitosan beads (IECBs) before and after adsorption.

pattern is associated with the fine size of the as-synthesized particles.

The XRD pattern of the IECBs is shown in Fig. 3b. The characteristic peaks at $2\theta = 35.2°$ and $63.82°$ corresponding to (311) and (440) crystallographic planes further confirmed the crystalline nature of the Fe_3O_4. The characteristic peak of chitosan is observed at $2\theta = 11°$ and $20°$.[42]

3.4 FTIR analysis

Fig. 3c shows the FTIR spectrum of the Fe_3O_4 nanoparticles. The broad bands observed at 580 cm^{-1} and 630 cm^{-1} are due to the vibrational stretching of Fe–O coordination bonds. The presence of hydroxyl groups is evident from broad peak bands at 3435 cm^{-1} and 1629 cm^{-1}, which originate from stretching and bending –OH functional groups, respectively.[43] Fig. 3d shows the spectra for IECBs before and after nitrate adsorption. The black line indicates the spectra of IECBs before adsorption, with the broad band observed at 616 cm^{-1} from the vibrational

stretching of Fe–O bonds. The absorption band at 1114 cm^{-1} shows that the Fe atoms are also connected to O atoms from the O–H functional groups. The peaks observed at 1626 cm^{-1} and 3424 cm^{-1} are due to the presence of N–H and O–H bonds, respectively.[44] The peaks observed at 2852 cm^{-1} and 2921 cm^{-1} are due to the C–H bonds in methyl (–CH_3–) and alkyl (–CH_2–) functional groups.[45] The red line shows the FTIR spectra of IECBs after nitrate adsorption. A broad absorption band observed at 1600 cm^{-1} is due to the N–O bonds of nitrate ions.[31]

3.5 Magnetic characteristics of IECBs

The magnetic characterization of the as-prepared IECBs is presented in Fig. S2.† The hysteresis loop is absent, which indicates the superparamagnetic behavior of IECBs. This curve is also evident due to the near-zero values of remanence magnetization ($M_r = 0.142$ emu per g) and the squareness ratio of $M_r/M_s = 0.004$. The present study reports a coercivity value of 12.23 Oe and a saturation magnetization (M_s) of ~33.2 emu

per g. The given values are closely similar to the literature values of PEG-coated nanoparticles (<50 nm) with saturation magnetization of 23 emu per g and M_r below 2 nm.[46] Another study of a similar material with particle size (50–300 nm) observed a coercivity value of 27 Oe and a M_r of 2.2.[47]

3.6 Influence of different single parameters on nitrate removal from water

The influence of the following parameters was investigated to understand the nitrate adsorption on IECBs: contact time, change in pH, mass of IECBs, and initial nitrate concentration.

3.6.1 Effect of time. Fig. 4a shows that nitrate adsorption increases significantly with time. First, the adsorption rate increases up to 120 min and then decreases until the saturation point is achieved. In the beginning, the adsorption rate increases due to the availability of many adsorption sites until most of the available sites are occupied by negatively charged nitrate (NO_3^-) ions. At this point, the remaining sites become difficult to fill due to the electrostatic repulsion between adsorbed and approaching ions. Then, saturation is achieved,

and nearly all the sites are occupied, resulting in no further nitrate adsorption.[20]

3.6.2 Impact of pH. pH is a key factor in the adsorption mechanism because it regulates the ionization behavior of the nitrate ions, surface potential and charge on the adsorbent's surface. Fig. 4b shows that the most suitable pH for nitrate removal is <5.5. This result agrees with a report by Tong *et al.* that the optimal pH range for nitrate removal is between 4 and 6.[38] They also reported that the point of zero charge of Fe_3O_4-chitosan IECBs was 6.94, indicating that under acidic conditions, the surface charge of the IECBs will be positive. In alignment with this reported behavior, our investigation also emphasizes that at pH levels below 6, the substantial removal of nitrate ions is attributed to the positively charged surface of the adsorbent, *i.e.*, IECBs. It is suggested that in an acidic environment, the heightened activity of H^+ ions could facilitate the adsorption of nitrate ions. Within this pH range, the positively charged IECB surface electrostatically attracts the negatively charged nitrate ions, optimizing the adsorption process. On the other hand, at pH > 7, the surface of the adsorbent becomes negatively charged, leading to electrostatic repulsion that
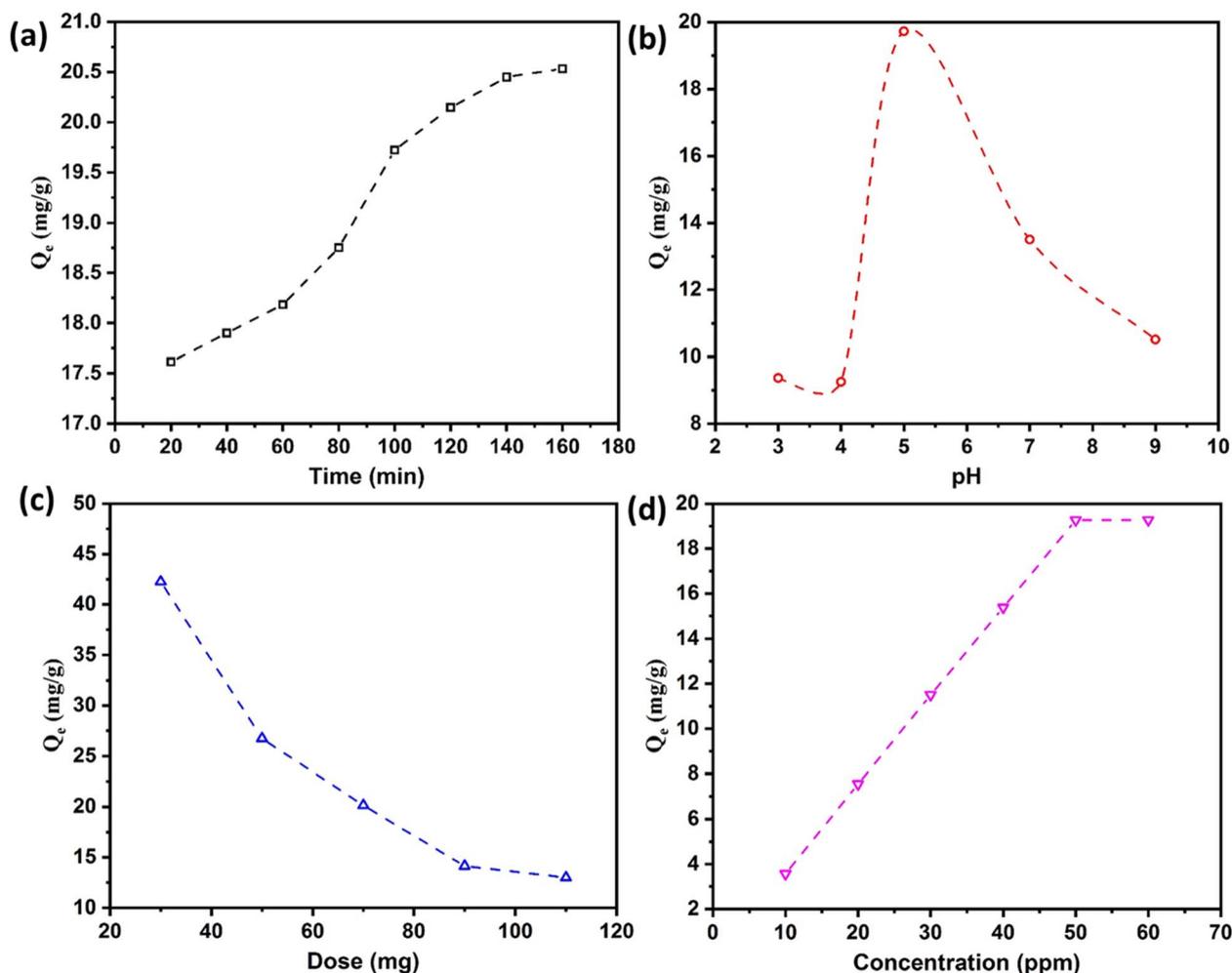

Fig. 4 Trends showing the effect of (a) time, (b) pH, (c) the bead dosage, and (d) initial nitrate concentration.

hinders the adsorption of nitrate ions onto the surface of IECBs.[48]

3.6.3 The effect of IECB mass loading. Fig. 4c shows that the nitrate removal rate increased significantly with an increase in IECBs. This is because increasing the dosage of IECBs provides an increased number of active sites for nitrate adsorption. For further adsorption studies, the IECB dose was arbitrarily fixed to 70 mg.

3.6.4 Impact of initial concentration. The influence of the initial nitrate concentration of the aqueous solution on the adsorption capacity of the IECBs is shown in Fig. 4. The adsorption onto the chitosan beads increased linearly with initial nitrate ion concentrations (Fig. 4d). This is because the initial concentration of nitrate ions affects the driving force for their adsorption on IECBs. A higher initial nitrate ion concentration facilitates their transport toward the adsorbent's surface

until saturation is achieved. Due to the reduction in the number of active adsorption sites, an equilibrium level of adsorption was seen at a concentration above 50 mg L^{-1}.[38]

3.7 Adsorption validation experiment

The adsorption capacities and nitrate removal efficiencies of the IECBs were also determined using eqn (1) and (2), respectively. All the data were used to plot the adsorption isotherms and adsorption kinetic models. The results show that for an optimum adsorption condition, when equilibrium is achieved after 2 h of stirring, the final concentration of nitrate in the solution was 0.414 mg L^{-1}, meaning that 93% of the solution's nitrate was adsorbed on the IECBs.

3.7.1 Adsorption mechanism of nitrate removal. In brief, magnetic beads are introduced into nitrate ion-containing
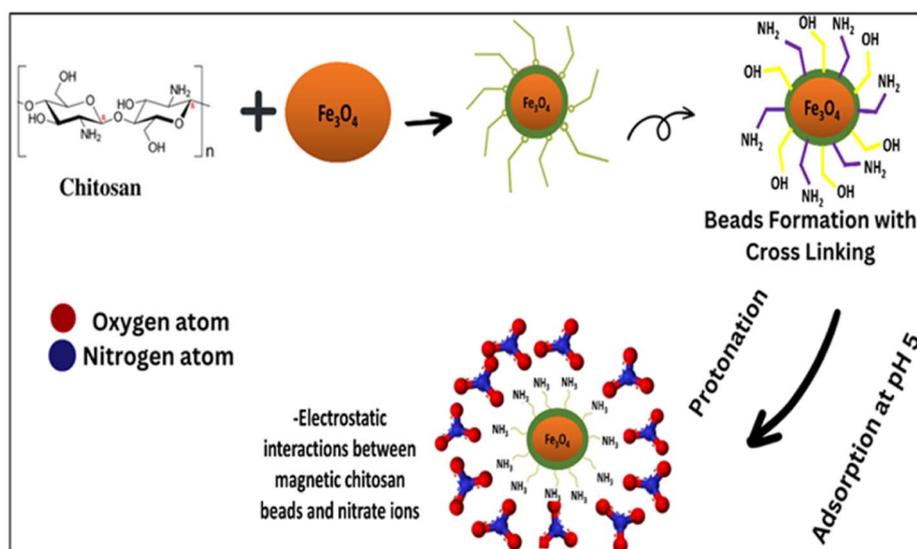

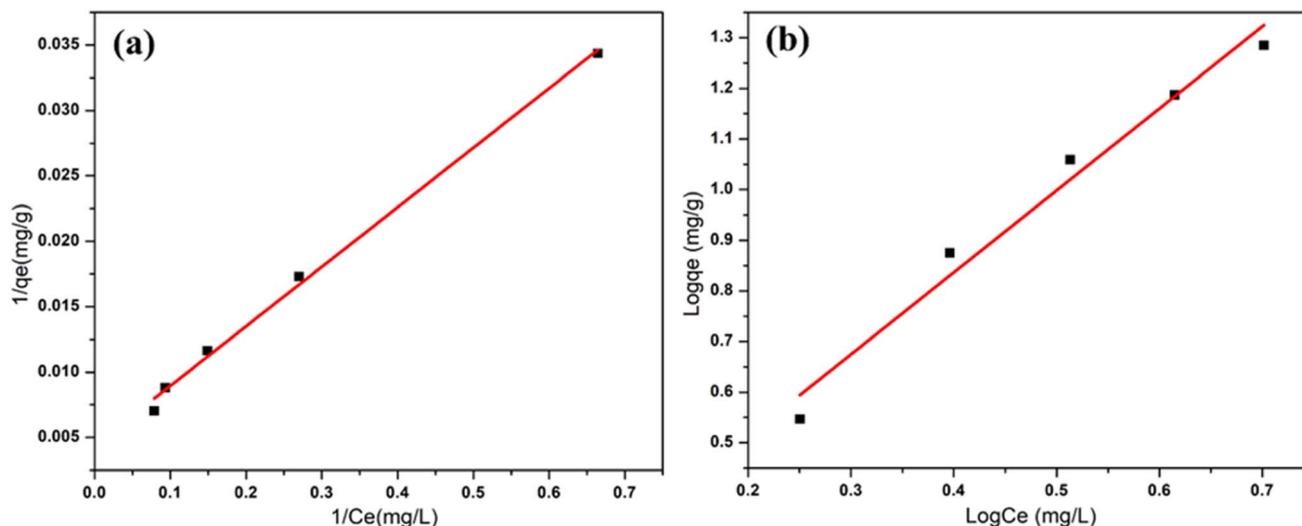Fig. 5 Schematic representation of the nitrate ion adsorption on the IECBs.

Fig. 6 Graphical representations of (a) Langmuir isotherm and (b) Freundlich isotherm model.

© 2024 The Author(s). Published by the Royal Society of Chemistry

Environ. Sci.: Adv., 2024, **3**, 572–584 | **579**

wastewater, attracting these ions to the bead surface through a combination of electrostatic interaction and chemical bonding. The mechanism of nitrate adsorption onto the beads is primarily based on electrostatic interactions between the positively charged IECBs and the negatively charged nitrate ions as shown schematically in Fig. 5. The surface of the IECBs containing hydroxyl (–OH) and amino (–NH$_2$) functional groups could interact with the nitrate ions through chemical bonding, such as coordination bonds or hydrogen bonding.[49,50] The nitrate ion adsorption is facilitated by the higher activity of H$^+$ ions under acidic conditions pH < 5.5 due to the protonation of the amino functional groups. This positive charge holds the nitrate ions on the surface of the IECBs electrostatically. Previous work has shown that the efficiency of nitrate removal using magnetic IECBs depends on several factors, *i.e.* size and surface area of the beads, type of the adsorbent material, pH of the wastewater, and nitrate ions concentration in wastewater.[51] Due to the magnetic nature of the Fe$_3$O$_4$ nanoparticles in the IECBs, the recovery of the loaded beads for stripping and reuse can be guaranteed through the application of a magnetic field.

3.7.2 Adsorption isotherms. The experimental data (conducted at room temperature) was assessed against Langmuir and Freundlich isotherms to discern whether the IECBs adsorb a monolayer of nitrate ions at homogeneous sites or multilayers at heterogeneous sites (Fig. 6). The regression values of these two models are given in Table 1. Comparing the R^2 values from the two models suggests that the adsorption behavior of this system likely aligns with the Langmuir isotherm. This is

Table 1 The regression values of Langmuir and Freundlich isotherm models

Langmuir isotherm model		Freundlich isotherm model	
Q_{max} (mg g^{-1})	5.29	K_F	0.91
K_L (L mg^{-1})	3.27	n	1.57
R^2	0.99	R^2	0.98

Table 2 Regression values of pseudo-first-order and second-order kinetic models

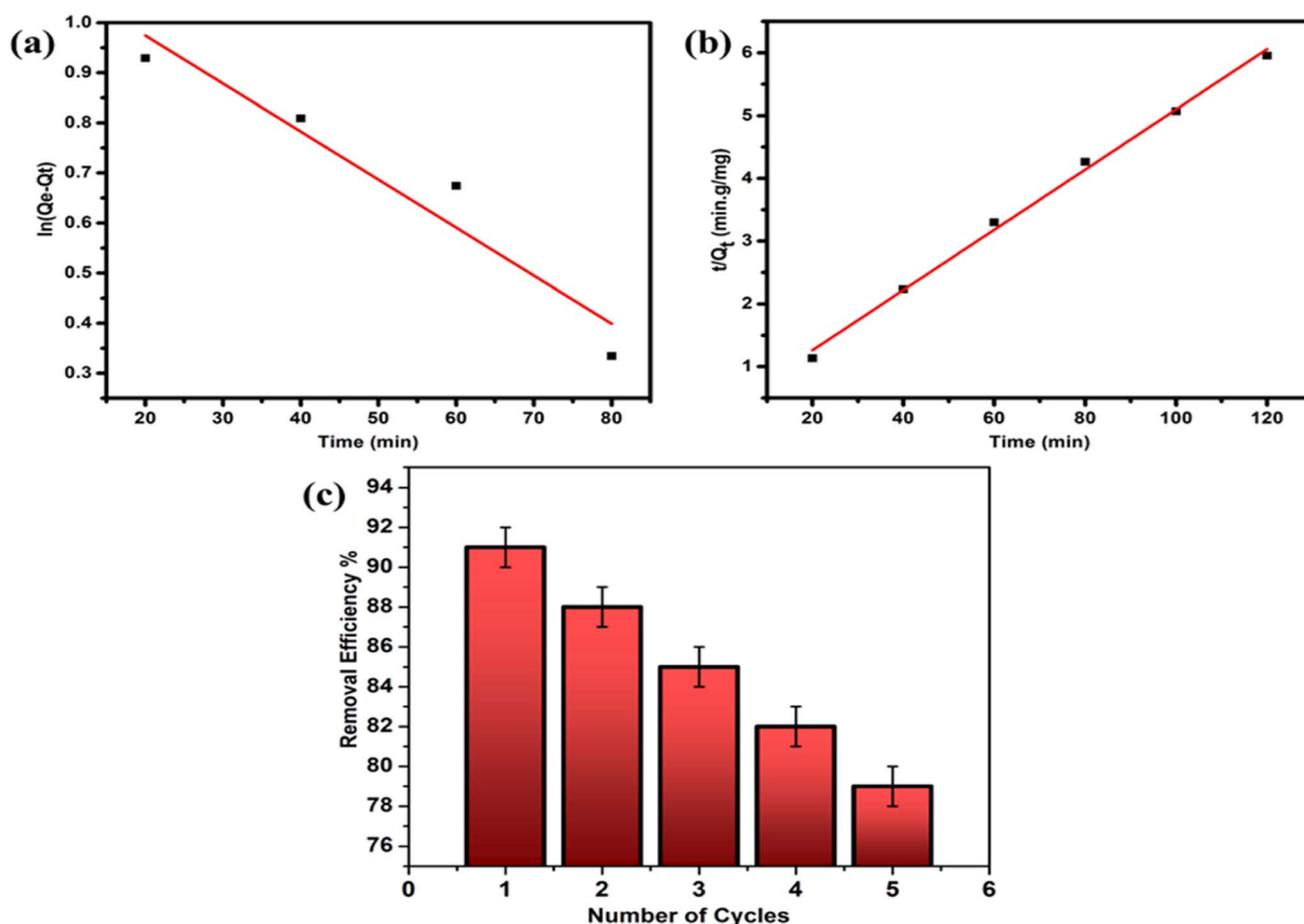| Pseudo-second first kinetic model		Pseudo second order kinetic model	
Q_e (mg g^{-1})	3.21	Q_e (mg g^{-1})	20.85
K_1	-2.4×10^{-4}	K_2 (h g mg^{-1})	15.9×10^{-4}
R^2	0.89	R^2	0.99

Fig. 7 Comparison of (a) pseudo-first-order, (b) pseudo-second-order kinetic model, and (c) the effect of regeneration cycles on the nitrate removal efficiency of IECBs.

Table 3 Comparison table of different sorbents with the present study for nitrate removal

Adsorbent materials	pH	Initial concentration (mg L^{-1})	Adsorption capacity (mg g^{-1})	Reference
Amine-modified cocoa shell adsorbent	5.5	50	12	52
Modified carbon aerogels	7	10–60	17.92	53
Modified CaCs	7	40–200	21.15	54
Modified chitosan microspheres	3	100	32.15	25
Magnetic iron oxide embedded chitosan beads	5	10–50	47.07	Present study

attributed to the negative charge of the monolayer at the outer surface of the beads, resulting in electrostatic repulsion to further approaching nitrate ions. Moreover, the R^2 value of the Freundlich isotherm model is also relatively close to unity, suggesting the localized multilayer adsorption of nitrates at active sites of the IECBs. On the other hand, the value of $n > 1$ indicates the homogeneous surface of the IECBs.

3.7.3 Adsorption kinetics. To confirm whether the nitrate adsorption on IECBs is governed by physisorption or chemisorption, the experimental data were compared and fitted to two adsorption kinetic models. Fig. 7a and b compare pseudo-first-order and second-order kinetic models, respectively. The adsorption rate is obtained based on two factors: the concentration of nitrate solution and the number of available sites for adsorption depending on the amount of IECB dosage. The rate constant K_2 is higher than K_1. The regression coefficient (R^2) values for these two models are listed in Table 2. The R^2 value for the pseudo-second-order (0.996) is very close to unity, unlike its value for the pseudo-first-order (0.895). Thus, it is evident from both Fig. 7 and Table 2 that the adsorption process is dominated by the pseudo-second-order kinetics model, which assumes that the nitrate ion adsorption on IECBs is based on chemisorption rather than physisorption.

3.8 Regeneration experiment

Adsorption/desorption cycles were repeated five times, and their effect on nitrate removal efficiency was studied. The results in Fig. 7c clearly indicate that the highest removal exceeds 91%. Subsequently, there is a gradual decline in the performance of the IECBs in each successive cycle, with their removal efficiency declining to 79% after the fifth regeneration cycle. Consequently, it can be inferred that IECBs are reusable for at least five cycles, with a marginal decline in efficiency during subsequent uses for nitrate removal. The plausible reason behind this observation could be the reduction in available active sites after successive cycles, leading to a decrease in adsorption. Table 3 provides a comparison between the reported IECBs and other adsorbent particles documented in the literature for effective nitrate removal.

The IECBs exhibit a notable adsorption capacity of 47.07 mg g^{-1}, surpassing other adsorbents. This is attributed to their elevated surface area and porous structure (as demonstrated in SEM) in comparison to similar adsorbents documented in the literature. The exceptional adsorption capacity of IECBs under optimal conditions is credited to electrostatic interactions and

hydrogen bonding facilitated by hydroxyl and amino functional groups, resulting in enhanced nitrate adsorption. This observation strongly aligns with pseudo-second-order kinetics.

4 Conclusions

Magnetic Fe$_3$O$_4$ nanoparticles were successfully synthesized *via* the co-precipitation route and subsequently embedded in chitosan to create beads for efficient adsorption of water pollutants, specifically targeting nitrate ions in wastewater. The beads (IECBs) were characterized using SEM, EDX, FTIR, BET, and XRD. SEM analysis revealed the formation of nearly spherical beads, and XRD confirmed the crystalline nature of Fe$_3$O$_4$ within the chitosan. In support of the SEM analysis, the presence of surface pores and high total pore volume of the embedded Fe$_3$O$_4$ particles within chitosan is confirmed from BET analysis. Adsorption studies were conducted utilizing adsorption isotherm and kinetic models. Comparative analysis of the experimental results revealed that the Langmuir model yielded the best fit with a higher regression coefficient value. This suggests that monolayer adsorption of nitrate ions at homogeneous surfaces predominates. Nevertheless, the possibility of multilayer adsorption at heterogeneous surfaces, like within the pores, cannot be disregarded, as indicated by Freundlich isotherm analysis. The adsorption kinetic model's experimental results exhibited the best fit with pseudo-second-order ($R^2 = 0.99$), suggesting a chemisorption adsorption process as a rate-determining step. The regeneration of the IECBs confirms their useability for 5 cycles, with a gradual decrease in nitrate removal efficiency from 93% to 79%. It is inferred that the developed IECBs can be regenerated for multiple cycles without a significant loss of removal efficiency. In conclusion, this study underscores the potential of IECBs as an effective adsorbent for the efficient and rapid removal of nitrate pollutants from wastewater.

Data availability

All data that support the findings of this study are included within the article (and any ESI files†). Further information can be obtained from the author(s) with a reasonable request.

Author contributions

Muntaha Nasir: experimental work, methodology, investigation, data analyses, writing – original draft. Farhan Javaid:

Conflicts of interest

The authors declare no conflict of interest.

Acknowledgements

References

1 A. S. Eltaweil, A. M. Omer, H. G. El-Aqapa, N. M. Gaber, N. F. Attia, G. M. El-Subruiti, M. S. Mohy-Eldin and E. M. Abd El-Monaem, Chitosan based adsorbents for the removal of phosphate and nitrate: A critical review, *Carbohydr. Polym.*, 2021, **274**, 118671.

2 E. Li, R. Wang, X. Jin, S. Lu, Z. Qiu and X. Zhang, Investigation into the nitrate removal efficiency and microbial communities in a sequencing batch reactor treating reverse osmosis concentrate produced by a coking wastewater treatment plant, *Environ. Technol.*, 2017, **39**, 1–43.

3 Y. Zhan, J. Lin and Z. Zhu, Removal of nitrate from aqueous solution using cetylpyridinium bromide (CPB) modified zeolite as adsorbent, *J. Hazard. Mater.*, 2011, **186**, 1972–1978.

4 R. Li, Y. Yuan, X. Zhan and B. Liu, Phosphorus removal in a sulfur-limestone autotrophic denitrification (SLAD) biofilter, *Environ. Sci. Pollut. Res. Int.*, 2013, **21**, 972–978.

5 B. Bishayee, R. P. Chatterjee, B. Ruj, S. Chakrabortty and J. Nayak, Strategic management of nitrate pollution from contaminated water using viable adsorbents: An economic assessment-based review with possible policy suggestions, *J. Environ. Manage.*, 2022, **303**, 114081.

6 H. A. T. Banu, P. Karthikeyan, S. Vigneshwaran and S. Meenakshi, Adsorptive performance of lanthanum encapsulated biopolymer chitosan-kaolin clay hybrid composite for the recovery of nitrate and phosphate from water, *Int. J. Biol. Macromol.*, 2020, **154,** 188–197.

7 D. E. Holmes, Y. Dang and J. A. Smith, Chapter Four - Nitrogen cycling during wastewater treatment, *Adv. Appl. Microbiol.*, 2019, **106**, 113–192.

8 F. Özyonar and M. U. Korkmaz, Sequential use of the electrocoagulation-electrooxidation processes for domestic wastewater treatment, *Chemosphere*, 2022, **290**, 133172.

9 J. Lakshmi, G. Sozhan and S. Vasudevan, Recovery of hydrogen and removal of nitrate from water by electrocoagulation process, *Environ. Sci. Pollut. Res.*, 2013, **20**, 2184–2192.

10 A. Lejarazu-Larrañaga, J. M. Ortiz, S. Molina, S. Pawlowski, C. F. Galinha, V. Otero, E. García-Calvo, S. Velizarov and J. G. Crespo, *Membranes*, 2022, **12**, 133172.

11 D. Li, X. Ning, Y. Yuan, Y. Hong and J. Zhang, Ion-exchange polymers modified bacterial cellulose electrodes for the selective removal of nitrite ions from tail water of dyeing wastewater, *J. Environ. Sci.*, 2020, **91**, 62–72.

12 X. Ma, M. Li, C. Feng and Z. He, Electrochemical nitrate removal with simultaneous magnesium recovery from a mimicked RO brine assisted by in situ chloride ions, *J. Hazard. Mater.*, 2020, **388**, 122085.

13 M. Yang, J. Wang, C. Shuang and A. Li, The improvement on total nitrogen removal in nitrate reduction by using a prepared $CuO–Co_3O_4/Ti$ cathode, *Chemosphere*, 2020, **255**, 126970.

14 M. Simonič, Reverse Osmosis Treatment of Wastewater for Reuse as Process Water—A Case Study, *Membranes*, 2021, **11**, 976–987.

15 H. Olvera-Vargas, N. Oturan, C. Aravindakumar, S. P. Menacherry, V. Sharma and M. Oturan, Electro-oxidation of the Dye Azure B: Kinetics, mechanism and by-products, *Environ. Sci. Pollut. Res. Int.*, 2014, **21**, 8379–8386.

16 A. Benhammada, D. Trache, M. Kesraoui and S. Chelouche, Hydrothermal Synthesis of Hematite Nanoparticles Decorated on Carbon Mesospheres and Their Synergetic Action on the Thermal Decomposition of Nitrocellulose, *Nanomaterials*, 2020, **10**(5), 968–987.

17 A. Lassenberger, T. Grünewald, P. Oostrum, H. Rennhofer, H. Amenitsch, R. Zirbs, H. Lichtenegger and E. Reimhult, Monodisperse Iron Oxide Nanoparticles by Thermal Decomposition: Elucidating Particle Formation by Second-Resolved in Situ Small-Angle X-ray Scattering, *Chem. Mater.*, 2017, **29**(10), 4511–4522.

18 M. Unni, A. Uhl, S. Savliwala, B. Savitzky, R. Dhavalikar, N. Garraud, D. Arnold, L. Kourkoutis, J. Andrew and C. Rinaldi, Thermal Decomposition Synthesis of Iron Oxide Nanoparticles with Diminished Magnetic Dead Layer by Controlled Addition of Oxygen, *ACS Nano*, 2017, **11**(2), 2284–2303.

19 D. Leybo, M. Tagirov, E. Permyakova, A. Konopatsky, K. Firestein, F. Tuyakova, D. Arkhipov and D. Kuznetsov, Ascorbic Acid-Assisted Polyol Synthesis of Iron and Fe/GO, Fe/h-BN Composites for Pb^{2+} Removal from Wastewaters, *Nanomaterials*, 2020, **10**(1), 37–57.

20 T. Dong, Nitrogen removal from groundwater using scoria: Kinetics, equilibria and microstructure, *J. Environ. Sci.*

Health, Part A: Toxic/Hazard. Subst. Environ. Eng., 2021, **56**, 1–8.

21 J. Sun, W. Xu, B. Cai, G. Huang, H. Zhang, Y. Zhang, Y. Yuan, K. Chang, K. Chen, Y. Peng and K. Chen, High-concentration nitrogen removal coupling with bioelectric power generation by a self-sustaining algal-bacterial biocathode photo-bioelectrochemical system under daily light/dark cycle, *Chemosphere*, 2019, **222**, 797–809.

22 J. Vymazal, Removal of nutrients in various types of constructed wetlands, *Sci. Total Environ.*, 2007, **380**, 48–65.

23 R. Prabhakar and S. Samadder, Use of adsorption-influencing parameters for designing the batch adsorber and neural network–based prediction modelling for the aqueous arsenate removal using combustion synthesised nano-alumina, *Environ. Sci. Pollut. Res.*, 2020, **27**, 26367–26384.

24 Y. Liu, X. Zhang and J. Wang, A critical review of various adsorbents for selective removal of nitrate from water: Structure, performance and mechanism, *Chemosphere*, 2022, **291**, 132728.

25 N. Mehrabi, M. Soleimani, M. Yeganeh and H. Sharififard, Parameter optimization for nitrate removal from water using activated carbon and composite of activated carbon and Fe_2O_3 nanoparticles, *RSC Adv.*, 2015, **5**, 51470–51482.

26 Z. Zareshahrabadi, M. Khorram, K. Pakshir, A.-M. Tamaddon, M. Jafari, H. Nouraei, N. T. Ardekani, N. Amirzadeh, C. Irajie, A. Barzegar, A. Iraji and K. Zomorodian, Magnetic chitosan nanoparticles loaded with Amphotericin B: Synthesis, properties and potentiation of antifungal activity against common human pathogenic fungal strains, *Int. J. Biol. Macromol.*, 2022, **222**, 1619–1631.

27 Q. Chen, M. Yang, X. Yang, H. Li, Z. Guo and M. H. Rahma, A large Raman scattering cross-section molecular embedded SERS aptasensor for ultrasensitive Aflatoxin B1 detection using $CS-Fe_3O_4$ for signal enrichment, *Spectrochim. Acta, Part A*, 2018, **189**, 147–153.

28 Q. Zeng, I. Baker, J. Loudis, Y. Liao and P. J. Hoopes, Synthesis and heating effect of iron/iron oxide composite and iron oxide nanoparticles – art. no. 64400H, *Proc. Soc. Photo-Opt. Instrum. Eng.*, 2007, **6440**, 13.

29 S. Pawar and A. Takke, Regulatory Aspects, Types and Bioapplications of Metallic Nanoparticles: A Review, *Curr. Drug Delivery*, 2023, **20**, 857–883.

30 S. Saqib, M. Farooq H. Munis, W. Zaman, F. Ullah, S. N. Shah, A. Ayaz and S. Bahadur, Synthesis, characterization and use of iron oxide nano particles for antibacterial activity, *Microsc. Res. Tech.*, 2019, **82**(4), 415–420.

31 P. Karthikeyan and S. Meenakshi, Fabrication of hybrid chitosan encapsulated magnetic-kaolin beads for adsorption of phosphate and nitrate ions from aqueous solutions, *Int. J. Biol. Macromol.*, 2021, **168**, 750–759.

32 S. Chatterjee and S. H. Woo, The removal of nitrate from aqueous solutions by chitosan hydrogel beads, *J. Hazard. Mater.*, 2009, **164**, 1012–1018.

33 M. P. Kesavan, S. Ayyanaar, V. Vijayakumar, J. Dhaveethu Raja, J. Annaraj, K. Sakthipandi and J. Rajesh, Magnetic iron oxide nanoparticles (MIONs) cross-linked natural polymer-based hybrid gel beads: Controlled nano anti-TB drug delivery application, *J. Biomed. Mater. Res., Part A*, 2018, **106**, 1039–1050.

34 J. Wu, X. Cheng, Y. Li and G. Yang, Constructing biodegradable nanochitin-contained chitosan hydrogel beads for fast and efficient removal of Cu(II) from aqueous solution, *Carbohydr. Polym.*, 2019, **211**, 152–160.

35 L. Ding, C. Guo, Y. Zhu, J. Ma, Y. Kong, M. Zhong, Q. Cao and H. Zhang, Adsorptive removal of gallic acid from aqueous solution onto magnetic ion exchange resin, *Water Sci. Technol.*, 2020, **81**(7), 1479–1493.

36 N. Lambert, P. Van Aken, R. Van den Broeck and R. Dewil, Adsorption of phosphate on iron-coated sand granules as a robust end-of-pipe purification strategy in the horticulture sector, *Chemosphere*, 2021, **267**, 129276.

37 W. M. Golie and S. Upadhyayula, An investigation on biosorption of nitrate from water by chitosan based organic-inorganic hybrid biocomposites, *Int. J. Biol. Macromol.*, 2017, **97**, 489–502.

38 X. Tong, Z. Yang, P. Xu, Y. Li and X. Niu, Nitrate adsorption from aqueous solutions by calcined ternary Mg-Al-Fe hydrotalcite, *Water Sci. Technol.*, 2017, **75**, 2194–2203.

39 Q. Hu, N. Chen, C. Feng, J. Zhang, W. Hu and L. Lv, Kinetic studies of nitrate removal from aqueous solution using granular chitosan-Fe(III) complex, *Water Sci. Technol.*, 2015, **73**, 1211–1220.

40 A. Hussain, A. Jadhav, Y.-K. Baek, H. Choi, J. Lee and Y. Kang, One Pot Synthesis of Exchange Coupled Nd2Fe14B/alpha-Fe by Pechini Type Sol-Gel Method, *J. Nanosci. Nanotechnol.*, 2013, **13**, 7717–7722.

41 R. P. Gambhir, A. K. Parthasarathy, S. Sharma, S. Kale, V. V. Magdum and A. P. Tiwari, pH-responsive glycine functionalized magnetic iron oxide nanoparticles for SARS-CoV-2 RNA extraction from clinical sample, *J. Mater. Sci.*, 2022, **57**, 13620–13631.

42 S. V. Durán, B. Lapo, M. Meneses and A. M. Sastre, Recovery of Neodymium (III) from Aqueous Phase by Chitosan-Manganese-Ferrite Magnetic Beads, *Nanomaterials*, 2020, **10**(6), 1204.

43 E. El-Monaem, M. Salah Ayoup, A. Omer, E. Hammad and A. Eltaweil, Sandwich-like construction of a new aminated chitosan Schiff base for efficient removal of Congo red, *Appl. Water Sci.*, 2023, **13**, 67.

44 A. S. Eltaweil, K. Ibrahim, E. M. Abd El-Monaem, G. M. El-Subruiti and A. M. Omer, Phosphate removal by Lanthanum-doped aminated graphene oxide@aminated chitosan microspheres: Insights into the adsorption mechanism, *J. Cleaner Prod.*, 2023, **385**, 135640.

45 E. El-Monaem, A. Omer and A. Eltaweil, Durable and Low-Cost Chitosan Decorated Fe/MOF-5 Bimetallic MOF Composite Film for High Performance of the Congo Red Adsorption, *J. Polym. Environ.*, 2023, 1–16.

46 R. Riaz, H. Waqar, N. Ahmad and S. R. Abbas, Novel Magnetic Elastic Phase-Change Nanodroplets as Dual

© 2024 The Author(s). Published by the Royal Society of Chemistry

Environ. Sci.: Adv., 2024, **3**, 572–584 | **583**

Mode Contrast Agent for Ultrasound and Magnetic Resonance Imaging, *Polymers*, 2022, **14**, 2915.

47 S. Khizar, N. Ahmad, H. Saleem, M. Hamayun, S. Manzoor, N. Lebaz and A. Elaissari, Magnetic Colloidal Particles in Combinatorial Thin-Film Gradients for Magnetic Resonance Imaging and Hyperthermia, *Adv. Polym. Technol.*, 2020, **2020**, 1.

48 D. Tibebe, A. Negash, M. Kassaw, Y. Kassa, Z. Moges and D. Y. Ayitegeb, Investigation of selected physico-chemical quality parameters in industrial wastewater by electrocoagulation process, Ethiopia, *BMC Chem.*, 2022, **16**, 67.

49 F. Ogata, N. Nagai, Y. Kariya, E. Nagahashi, Y. Kobayashi, N. Takehiro and N. Kawasaki, Adsorption of Nitrite and Nitrate Ions from an Aqueous Solution by Fe–Mg-Type Hydrotalcites at Different Molar Ratios, *Chem. Pharm. Bull.*, 2018, **66**, 458–465.

50 N. Öztürk and T. E. Bektaş, Nitrate removal from aqueous solution by adsorption onto various materials, *J. Hazard. Mater.*, 2004, **112**, 155–162.

51 Q. Chang, A. Ali, J. Su, Q. Wen, Y. Bai and Z. Gao, Simultaneous removal of nitrate, manganese, and tetracycline by Zoogloea sp. MFQ7: Adsorption mechanism of tetracycline by biological precipitation, *Bioresour. Technol.*, 2021, **340**, 125690.

52 P. Nkuigue Fotsing, N. Bouazizi, E. Djoufac Woumfo, N. Mofaddel, F. Le Derf and J. Vieillard, Investigation of chromate and nitrate removal by adsorption at the surface of an amine-modified cocoa shell adsorbent, *J. Environ. Chem. Eng.*, 2021, **9**, 104618.

53 N. Raeisi Kheirabadi, N. Salman Tabrizi and P. Sangpour, Removal of Nitrate from Water by Alginate-Derived Carbon Aerogel Modified by Protonated Cross-Linked Chitosan, *J. Polym. Environ.*, 2019, **27**, 1642–1652.

54 M. Mazarji, B. Aminzadeh, M. Baghdadi and A. Bhatnagar, Removal of nitrate from aqueous solution using modified granular activated carbon, *J. Mol. Liq.*, 2017, **233**, 139–148.